## Chapter 4 Instabilities induced by small pump size

It is commonly believed that spontaneous instabilities are impossible in class B lasers described by simple two-level rate equations without an additional degree of freedom such as external modulation, light injection, delayed feedback, etc. [1]. However, the transverse effects such as gain variation and diffraction in the resonator provide the additional degree of freedom and have been demonstrated to play important roles in lasers [2,3]. Because various transverse modes may be excited especially when the laser is operated at near-degeneracy, a degenerate resonator is thus a good choice for obtaining laser instabilities. Previously, we have analyzed an iterative map of the q-parameter of the resonator [4] and concluded that a laser will become unstable near some degenerate cavity configurations under nonlinear effects. Using an end-pumped cw Nd:$YVO_4$ laser, we have studied different laser behaviors under various pump sizes [5,6] when the cavity is near 1/3-transverse degeneracy ($g_1g_2 = 1/4$). Recently, the Petermann K factor has also been calculated for maxima on each side of the degeneracy under strong gain guiding or small pump size [7]. It was emphasized that in the vicinity of the degeneracies the empty-cavity degenerate transverse modes are phase-locked and the resultant radial phase profile depends strongly on the cavity-length detuning.

In this chapter, we study the cavity-configuration-dependent instability and determine the unstable regions with cavity length, pump power, and pump size as the control parameters. When the pump size is small, we found that the laser always exhibits a stable cw output, except for a narrow range of cavity tuning on each side of the degeneracy. The temporal behaviors of the laser output show periodic, period-doubling, and chaotic evolutions. We also observed various patterns in the far field when we scanned the cavity length. In particular, an anomalous mode

pattern is accompanied with frequency beating close to the point of degeneration. The simulation by the use of Collin's integral and rate equations, while taking into account the thermal lens effect, shows good agreement with the experiment. The observed instabilities are new and, as far as we know, this is the first report that discusses the relationship between the instability and the thermal lens effect.

## 4.1 Experimental setup

The experimental setup that is similar to Fig. 3.1 is schematically shown in Fig. 4.1. The plano-concave cavity and the Nd:$YVO_4$ crystal are the same as in Fig. 3.1. The OC of 10 % transmission was mounted upon a translation stage so we could tune the cavity length (L) near the degenerate configuration. The degeneration point of $g_1g_2$ = 1/4, which corresponds to L = 6 cm, was determined by the cavity length where the lowest lasing threshold occurs [8]. The laser output was split into two beams, one of which was recorded by a CCD camera and the other was further split into two beams that were individually collected by two photodiodes (PDs) with rise times < 0.3 ns. The signals of the PDs were then fed into a LECROY-9450A oscilloscope (bandwidth 200 MHz) and an HP8560E rf spectrum analyzer (bandwidth 2.9 GHz), respectively. The Gaussian pump radius, $w_p$, was determined by the standard knife method. The 1/3-degeneration (or $g_1g_2$ = 1/4) point L = 6 cm was determined by the position where the lowest lasing threshold occurs [2,3].

## 4.2 Experimental results

### 4.2.1 Unstable regions

The output power varied with the cavity length under various pump radii and is shown in Fig. 4.2(a). The bottom three curves for $w_p$ = 19 μm show that a higher pump power not only widens but also heightens the power hump. The laser exhibits

a stable cw output for almost entire range of the studied 3-mm cavity tuning. However, within a narrow range of L on each side of the power hump, denoted as stars in Fig. 4.2(a), we always observed spontaneous instabilities. The top two curves are the cavity-length-dependent output power for $w_p$ = 25 μm and 34 μm at a pump power of 300 mW, in which the triangles and the solid circles denote the unstable regions for both cases. Note that the radius of cold-cavity fundamental mode is approximately 108 μm. Summarized in Fig. 4.2(b) are the unstable regions in terms of the cavity length and the pump power for the three pump sizes of 19 μm, 25 μm, and 34 μm. We use a single symbol to denote a narrow unstable region while twin symbols are used to encompass a wider unstable region of about 100 μm. One can see that the unstable regions on the short-cavity side are well separated for different $w_p$ and located farther away from degeneracy with increasing the pump power; in contrast, those on the long-cavity side are located very close to the point of degeneration and are nearly independent of the pump power.

4.2.2 Far-field patterns

When the cavity length was tuned from the long-cavity side, toward and across the point of degeneration, various far-field mode patterns were observed. The mode pattern shows a near-fundamental Gaussian distribution far from degeneracy. Tuning L close to the right edge of the unstable region, we observed a slightly distorted mode pattern. When the cavity was set within about 100 μm of the unstable region, the mode pattern became non-cylindrically symmetric and strongly spread in a special direction as shown in Fig. 4.3(a). This anomalous spreading pattern maintained wider than the whole unstable region by few tens of micrometers. When L was tuned across the range that showed the spreading pattern, the far-field pattern recovered to a cylindrically symmetric one but turned into many concentric

rings with a dark center that is the far-field pattern of the multi-beam-waist mode [6]. By further tuning of L toward the unstable region on the short-cavity side, we observed the cylindrically symmetric mode pattern as shown in Fig. 4.3(b) that differs from the patterns in the unstable region of the long-cavity side, as indicated in Fig. 4.3(a).

4.2.3 Temporal behaviors and spectra

We further investigated the temporal behaviors of the output power within the unstable regions at $P_{pump}$ = 260 mW and $w_p$ = 34 μm. Figure 4.4(a) shows a periodic time trace when the cavity was tuned at the edge of the long-cavity unstable region. Its corresponding rf spectrum in Fig. 4.4(b) shows one main peak at 1.33 MHz and three harmonics. When the cavity length was decreased by ~20 μm from the position of Fig. 4.4(a), a period-2 evolution was observed. The time trace and its spectrum are shown in Figs. 4.4(c) and 4.4(d), respectively. On continuing the decreasing of the cavity length, we recorded a chaotic evolution in Fig. 4.4(e) with a broad low frequency spectrum indicated in Fig. 4.4(f). Calculation by use of the chaos data analyzer (American Institute of Physics) shows that the correlation dimension of the chaotic evolution is approximately 2.1.

Although the temporal behaviors of the cavity-configuration-dependent instabilities are similar on each side of the degeneracy, the high-frequency responses of their power spectra are quite different. For the long-cavity instabilities we observed multiple beating frequencies at 812 MHz, 1.63 GHz, and 2.44 GHz [see Fig. 4.4(g)] that were confirmed with a Fabry-Perot interferometer (FPI) having FSR = 15 GHz and finesse = 150. The transverse mode beating pertaining to the Laguerre-Gaussian $LG_{1,0}$ and/or $LG_{2,0}$ modes would induce spatiotemporal instability, where the subscripts 1 and 2 are the radial indices and 0 is the azimuthal index.

However, within the short-cavity unstable region the spectrum shows only the longitudinal mode beating at 2.44 GHz with the absence of transverse mode beating in both of the rf and the FPI spectra.

To investigate the distinction between the instabilities on the long-cavity side and those of the short-cavity side, we used two PDs at different transverse positions to simultaneously record the laser power. The first PD was fixed at the center of the profile as reference and the second one was located at an off-axis position. When the two detectors were separated within a distance, their temporal traces on the oscilloscope were completely the same as shown in Fig. 4.5(a). However, we found for the long-cavity instability that the high peak of one trace coincided with the low peak of the other trace as shown in Fig. 4.5(b) when the two detectors were separated by some specific distance. This reveals that the intensity profile varies with time and thus indicates spatiotemporal instability. On the other hand, within the short-cavity unstable region, we always observed the same behavior between the two signals no matter at what position the second PD was located. Temporal instability was exhibited on the short-cavity side. In addition, we also found that the instabilities on both sides of the degeneracy are closely related to high-order transverse modes because the instabilities disappeared when a knife-edge was inserted ~500 μm into the cavity beam to inhibit the high-order transverse modes. This will be explained in the following section.

## 4.3 Numerical model

The model has been described in Section 2.1 except we imposed the phase shift $\Delta\Phi$ induced by thermal lens effect in the Collin integral. The phase shift is given [5] by

$$\Delta\Phi(r') = \int_0^d k\,\Delta T(r',z)\,\frac{dn}{dT}dz \quad , \tag{4.1}$$

where $\Delta T(r',z) = -\frac{1}{K_c}\int_{r'}^{r_b}\frac{\alpha\xi P_{abs}}{2\pi}\exp(-\alpha z)\frac{1-\exp(-2r^2/w_p^{\,2})}{r}dr$ is the temperature difference between the calculated point (r', z) and the boundary point ($r_b$, z), ξ is the fractional thermal loading, $P_{abs}$ is the absorbed pump power, z is the axial coordinate, and $r_b$, d, α, $K_c$, and dn/dT are the radius, thickness, absorption coefficient, thermal conductivity, and the thermal-optic coefficient of the laser crystal, respectively. Note that the contribution of the thermal induced stress and the thermal deformation of the crystal are neglected and the conventional edge cooling is assumed. Thus the Collin integral is written as

$$E^{-}_{m+1}(r) = \frac{2\pi i}{B\lambda}\int_0^{\infty}\exp(-\frac{i2\pi 2L}{\lambda} - i\Delta\Phi(r'))E^{+}_{m}(r')\exp\{-(\frac{i\pi}{B\lambda})(A\,r'^2+D\,r^2)\}J_0(\frac{2\pi rr'}{B\lambda})r'\,dr' \tag{4.2}$$

with round trip transmission matrix $M = \begin{bmatrix} A & B \\ C & D \end{bmatrix}$. The rate equation [see Eq. (2.3)] and the relations for amplification of the field [see Eq. (2.2)] are the same as in Section 2.1. The total pumping rate over the entire active medium is

$$\int_V R_{pm}dV = P_p / h\nu_p \quad , \tag{4.3}$$

where $P_p$ is the effective pumping power which equals to $(1-\xi)P_{abs}$, $h\nu_p$ is the photon energy of the pumping laser, and the integral is integrated for the pump volume. Therefore, we have three control parameters L, $w_p$ and $P_p$ if ρ is fixed.

Given an initial ΔN and E, the field evolution will converge to a stationary solution if the final state is stable cw. Contrarily, if the final state is unstable, the E field will automatically evolve to a dynamical state. To obtain the time evolution of the output power, we set the reference plane with 600 μm aperture at the flat end

mirror and laterally integrated the intensity profile for each round trip.

## 4.4 Numerical results

### 4.4.1 Unstable regions

The parameters that we used are $\xi = 0.23$, $\alpha = 1930\ m^{-1}$, $K_c = 5.23\ Wm^{-1}K^{-1}$, $dn/dT = 8.5\times10^{-6}\ K^{-1}$, and the others are the same as described in chapter 3. Figure 4.6(a) shows the output power as a function of L when considering the thermal lens effect. The curves of output power that are labeled as triangles, empty squares, and solid circles for $w_p = 25\ \mu m$, $30\ \mu m$, and $35\ \mu m$ respectively show asymmetric power humps with respect to the point of degeneration. The dependence of the power hump on $w_p$ and $P_p$ (the effective pump power) are the same as in Fig. 4.2(a). The unstable regions are summarized for four values of $w_p$ in Fig. 4.6(b), which are similar to those in Fig. 4.2(b) except that the vertical axis of Fig. 4.6 is the effective pump power that matches with the pump efficiency of ~0.6 taken from the measured pumping. Again, in Fig. 4.6(b) we use a single symbol to denote a narrow unstable region while twin symbols are used to encompass a wider unstable region. It shows similar unstable regions and dependence on $w_p$ and $P_p$ as those in Fig. 4.2(b); for example, at $w_p = 35\ \mu m$, the unstable region shifts approximately from L = 5.94 cm to 5.90 cm on the short-cavity side as one increases the effective pump power to match with the experiment data in Fig. 4.2(b). Moreover, the far-field intensity profiles beside the long-cavity unstable region are similar to those in Fig. 2(b) of Ref. 6. In addition, no instability can be observed as $w_p > 40\ \mu m$, which is also consistent with the experiment.

To study the influence of the thermal lens effect, we repeated the simulation without considering the thermal lens effect. The calculated output power and the obtained unstable regions are shown in Figs. 4.7(a) and 4.7(b), respectively. As

compared with Fig. 4.6, we found the thermal lens effect leads to certain phenomena: (1) an asymmetrical shape of the power hump; (2) asymmetrical unstable regions with respect to the degeneration point; (3) dependence of the region shift on $P_p$ on the short-cavity side but not on the long-cavity side; and (4) much less shift of the power maximum than shift of the unstable region (e.g., see $w_p$ = 30 μm and $P_p$ = 150 mW).

4.4.2 Temporal behaviors and the origin of the instabilities

Without the thermal lens effect, not only the power hump but also the dynamical behaviors are symmetric with respect to the point of degeneration. The simulated temporal evolution of the unstable output power exhibits self-pulsation on both sides of the degeneracy with a pulsing frequency of few hundred kHz [see Fig. 4.8(a)]. The simulated intensity profile of each round trip show the variation of the on-axis peak intensity with time as the characteristic feature of Fig. 4.8(a), but the normalized profile varies only a little. We plotted four normalized intensity profiles in Fig. 4.8(b) from the pulse peak to valley to show the variation. Their corresponding far-field intensity profiles [insets in Fig. 4.8(b)], having two obvious rings, agree with the photograph of Fig. 4.3(b). Moreover, the far-field intensity profile decreases smoothly and then increases when the pulse is growing. This leads to pure temporal instability. The modal analysis shows that the modes in Fig. 4.8(b) can be decomposed into the combination of the near-degenerate $LG_{0,0}$, $LG_{3,0}$,…, $LG_{18,0}$ modes with mode weights and relative phase shifts because $LG_{21,0}$ undergoes large diffraction losses for a 600 μm aperture at the reference plane. These phase shifts must be included because the phase pattern is important as emphasized in Ref. 7. We give a fitted result in the figure caption of Fig. 4.8(b). When the thermal lens effect is included, the feature of self-pulsation is unchanged for the short-cavity side. This matches with the general expectation that the thermal lens effect will only shift

the cavity length.

However, on the long-cavity side the region shift seems independent of $P_p$ and the self-pulsation becomes the characteristic feature of Fig. 4.8(c), in which the output power forms three branches of oscillation. The first 20 iterations in the inset show that the output evolution nearly comes back the same value after three round trips; that is the power spectrum indicates one peak at roughly 1/3-longitudinal beating frequency that corresponds to the experimental data of 812 MHz. The intensity profiles of three successive round trips are shown in Fig. 4.8(d), which are not normalized due to the large difference. The corresponding far-field intensity profiles in the inset of Fig. 4.8(d) exhibit a complex feature, which is different from that of the short-cavity side. Unfortunately, we could not yet obtain good fitting data by running the same fitting parameters, even when the $LG_{1,0}$ mode was included. This may be due to the peculiar phase pattern that is deformed strongly by the thermal lens effect in the vicinity of the degeneracy. Because the beating frequency between the near-degenerate LG modes are absent on both long-cavity and short-cavity instabilities, the frequencies of the near-degenerate LG modes are locked together to a single frequency. Therefore the frequency-locked mode, a supermode [13], interacts with the inverted populations and thus leads to the short-cavity instabilities. However, the long-cavity instabilities arise mainly from the frequency beating between the supermode and the other empty-cavity modes. Although the asymmetric (spreading) mode pattern of Fig. 4.3(a) cannot be produced by using the cylindrically symmetric model with single optical frequency, the simulated results agree with the experiment of transverse mode beating. As far as we know, this is the first report that discusses the relationship between the instability and the thermal lens effect.

Furthermore, when the aperture on the reference plane is decreased to 450 μm, in

accordance with the experiment described in Section 2, the instability disappears. The stationary mode now consists of the near-degenerate LG modes with the same frequency but lack of the higher-order $LG_{15,0}$ and $LG_{18,0}$ modes. This fact of transverse mode locking was confirmed by the absence of the near-degenerate mode beating and by the observation of the intensity profile variation with the propagation distance as done in Ref. 6. The supermode lack of the components of the $LG_{15,0}$ and $LG_{18,0}$ modes is unable to arise the instability. Inserting a knife-edge into the cavity beam in our experiment also results in a cylindrically symmetric pattern instead of a spreading pattern. Apparently, the high-order modes with small amplitude may play important roles in symmetry breaking as indicated in Ref. 14. However, the origin of the symmetry breaking is still unknown.

4.4.3 Transverse mode locking

In mode expansion we decomposed the gain-guided mode into $LG_{p,0}$ modes with p = 0, 3, 6, …18. The mode weight of the $LG_{0,0}$ mode is fixed unity and the other six are limited between 0 and 1 and their relative phase shifts are between $-\pi$ and $\pi$ for these LG modes. Both of the intensity profile and the phase pattern are fitted well. We show in Fig. 4.9 for the degenerate case of L = 6.0 cm without the thermal lens effect. In Figs. 4.9(a) and 4.9(b) the solid circles and the open circles are respectively the results of mode calculation and the fitted mode expansion. The central lobe of the intensity profile is near-Gaussian with the waist radius of ~30 μm (see the solid curve in the inset of Fig. 4.9(a) with linear scale) approximately equals to the pump radius, which shows that the laser is strongly gain-guided. The seriously saturated gain distribution is also shown with the dashed curve in the inset of Fig. 4.9(a). Figure 4.9(b) shows that the phase pattern is flat within r = 200 μm but discontinuously jumps $\pi$ phase at some positions of r. The first phase jump at

r = 200 μm corresponds to the position of the second intensity zero of the $LG_{3,0}$ mode, where 3 is the radial mode index and 0 is the azimuthal index. The fitted data [also see Fig. 4.10] for L = 6.0 cm shows the degenerate empty-cavity LG modes are not only phase-locked but also nearly in-phase at the reference plane.

Since the mode is phase-locked, its intensity profile will vary with the propagation distance due to the Gouy phase of the $LG_{p,0}$ mode being (2p+1) $\arctan(z/z_R)$, where $z_R$ is the Rayleigh length and z is propagation distance from the reference plane. The simulation of the propagation behavior has been shown in Fig. 3(a) of Ref. 6 but we did not understand it by mode expansion. We know here that the in-phase position of z is located at $\sqrt{3}z_R \sim 6$ cm where the second waist will be formed. Out-of-phase between $LG_{0,0}$ and $LG_{3,0}$ occurs at the positions of $z \sim z_R / \sqrt{3} = 2$ cm and at the far field, where the intensity profile has a dark center. Three beam waists can be observed as described in chapter 3 when a simple convergent lens is set behind the output coupler.

When the cavity length is tuned to L = 6.01 cm, the intensity profile and the phase pattern are shown in Figs. 4.9(c) and 4.9(d), respectively. The central lobe of the intensity profile is a slightly distorted Gaussian that is shown in the inset of Fig. 4.9(c) with the solid curve using linear scale. Also shown with the dashed curve in the inset is the saturated gain distribution. We can see in Fig. 4.9(d) that the phase pattern is already highly curved for r < 100 μm and no longer jumps $\pi$ at some positions of r. Note that the phase jump at r = 223 μm is $2\pi$, so it is a continuous phase. The fitted result in Fig. 4.10 for L = 6.01 cm shows that the empty-cavity LG modes are no longer in-phase at the reference plane but have monotonically increasing relative phases with the increase of the radial mode index. Even so, these empty-cavity LG modes are still phase-locked and the Gouy phase variation with z

still results in the multi-beam waists. It is worthy to note that nearly the same behavior for the case of L = 5.99 cm except that the phase pattern is inverted within r = 100 μm. So the fitted relative phases of the LG modes decrease monotonically with the increase of the radial mode index.

The fitted mode weights and the relative phases of the LG modes are summarized in Fig. 4.10(a) and 4.10(b) when L is tuned away from the degeneracy, where the case of L = 6.04 cm is absent because the laser instability occurs there. For $w_p$ = 30 μm and L = 6.04 cm, the simulations show the intensity profile [see Fig. 4.8(b)] and the phase pattern vary with time approximately between those of L = 6.03 cm and those of L = 6.05 cm. We may understand the amplitude and phase variation of the LG modes from Fig. 4.10. We see that the mode weights for the case of L = 6.05 cm have meaningful decrease for p = 3, 6, 9 as compared with that of L = 6.03 cm and that the relative phases no longer monotonically increase but alternate for p > 6.

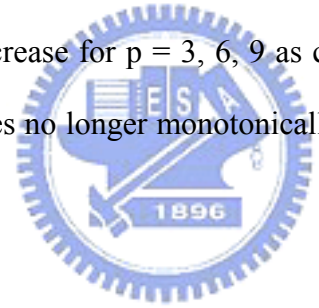

4.4.4 Discussions

Going back to Fig. 4.8(a), the pulsation is damped by the relaxation oscillation so the pulsing frequency depends on the pump power and the cavity length. Theoretically, the pulsing spectrum can be calculated from the Fourier transform of the output power evolution. Interestingly, by using $\gamma = 1\times10^5 s^{-1}$ we obtained periodic pulsing [Figs. 4.11(a) and 4.11(b)], period-2 [Figs. 4.11(c) and 4.11(d)], and chaotic [Figs. 4.11(e) and 4.11(f)] time evolution of the output power when L was tuned from 5.96 cm to 5.951 cm with $w_p$ = 30 $\mu$m and an effective pump power of 100 mW. For L = 5.948 cm a homoclinic orbit shown in [Figs. 4.11(g) and 4.11(h)] was clearly seen in the phase portrait reconstructed from the standard time-delay technique. The routes to chaos both through Hopf bifurcation and through

intermittency associated with the homoclinic orbit were shown in an end-pumped standing-wave alexandrite laser [15]. It is possible that our laser performs homoclinic dynamics because our simulation is consistent with the experiment and this needs further be studied

References

[1] C.O. Weiss, R. Vilaseca, Dynamics of lasers (VCH, New York, 1991).

[2] L.A. Lugiato, F. Prati, L.M. Narducci, P. Ru, J.R. Tredicce, D.K. Bandy, Phys. Rev. A 37, 3847(1988).

[3] L.A. Lugiato, G.L. Oppo, J.R. Tredicce, L.M. Narducci, M.A. Pernigo, J. Opt. Soc. Am. B 7, 1019 (1990).

[4] M.D. Wei, W.F. Hsieh, C. C. Sung, Opt. Commun. 146, 201(1998).

[5] C.H. Chen, M.D. Wei, W.F. Hsieh, J. Opt. Soc. Am. B 18, 1076 (2001).

[6] C.H. Chen, P.T. Tai, M.D. Wei, W.F. Hsieh, J. Opt. Soc. Am. B 20, 1220 (2003).

[7] C.F. Maes, E.M. Wright, Opt. Lett. 29, 229 (2004).

[8] H.H. Wu, W.F. Hsieh, J. Opt. Soc. Am. B 18, 7 (2001).

[9] S.A. Collins, J. Opt. Soc. Am. 60, 1168 (1970).

[10] F. Hollinger, Chr. Jung, J. Opt. Soc. Am. B 2, 218 (1985).

[11] Y.J. Cheng, P.L. Mussche, A.E. Siegman, IEEE J. Quantum Electron. 31, 391 (1995).

[12] M.E. Innocenzi, H.T. Yura, C.L. Fincher, R.A. Field, Appl. Phys. Lett. 56, 1831 (1990).

[13] E.J. D'Angelo, C. Green, J.R. Tredicce, N.B. Abraham, S. Balle, Z. Chen, G.L. Oppo, Physica D 61, 6 (1992).

[14] H. Lin, N.B. Abraham, Opt. Commun. 79, 476 (1990).

[15] W. Gadomski, B. Ratajska-Gadomska, J. Opt. Soc. Am. B 17, 188 (2000).

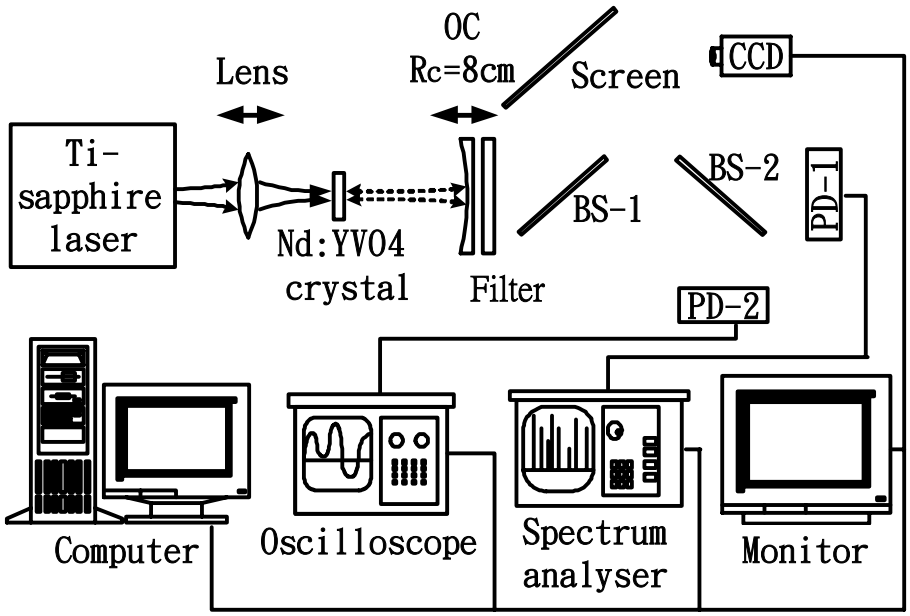


Fig. 4.1. The schematic of experimental set up. BS is the beam

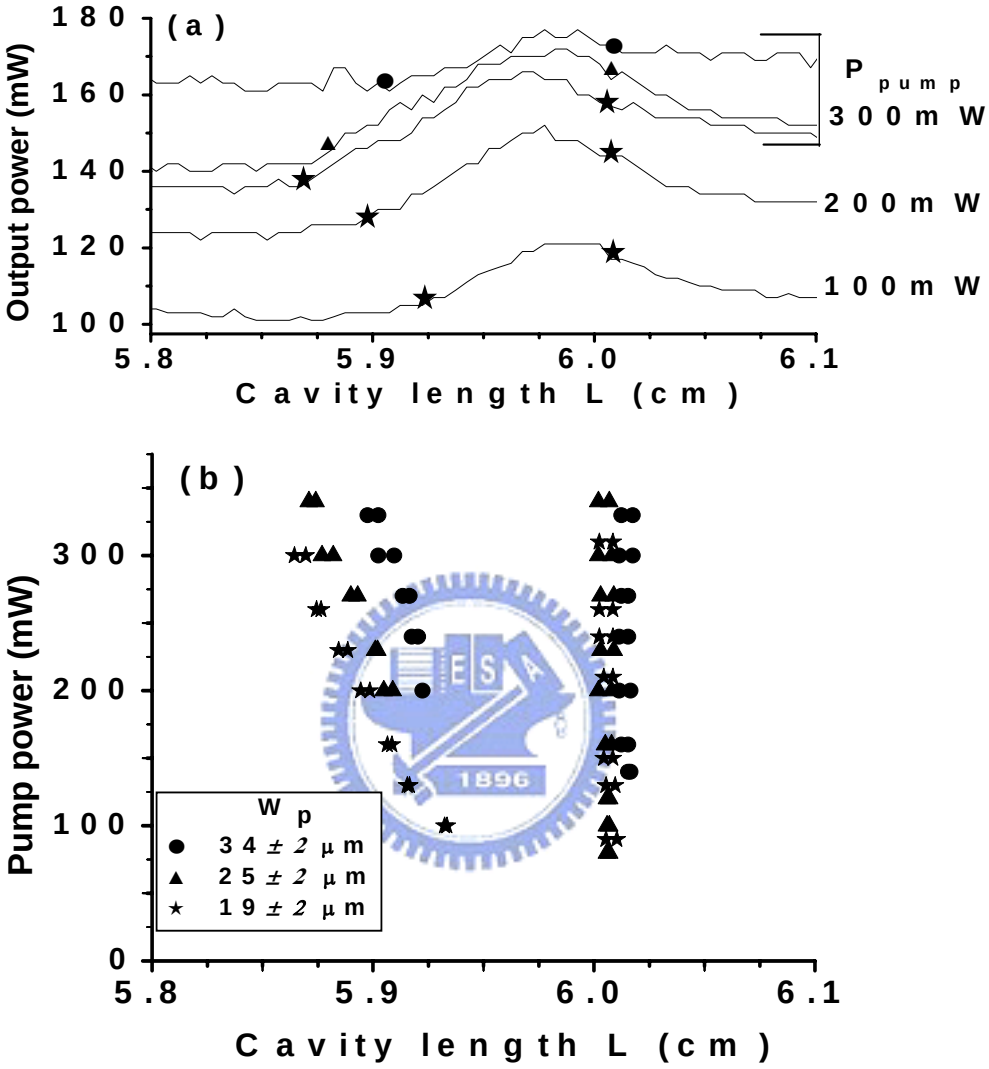


Fig. 4.2. The observed output power as a function of cavity length (a) and the unstable regions in terms of the cavity length and the pump power for different $w_p$ (b). The symbols for $w_p$ are the same in (a) and (b). The output power is around 40 mW for $P_{pump}$ = 100 mW as $w_p$ = 19 μm. Note that we have added 50 mW and 75 mW for the curves of $P_{pump}$ = 200 mW and $P_{pump}$ = 100 mW. The absorption efficiency of $P_{pump}$ is about 60 - 70%. The lasing threshold is about 5 – 30 mW depending on L and $w_p$.

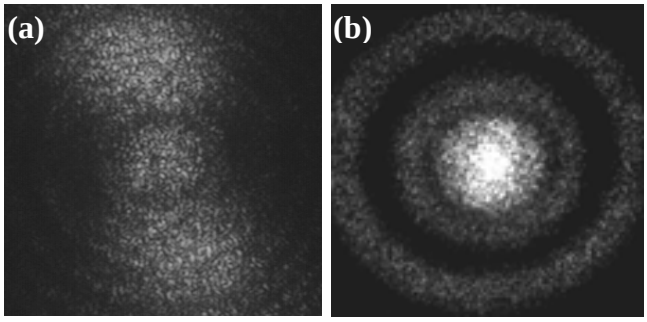


Fig. 4.3. The far-field mode patterns inside the long-cavity unstable region (a) and inside the short-cavity unstable region (b).

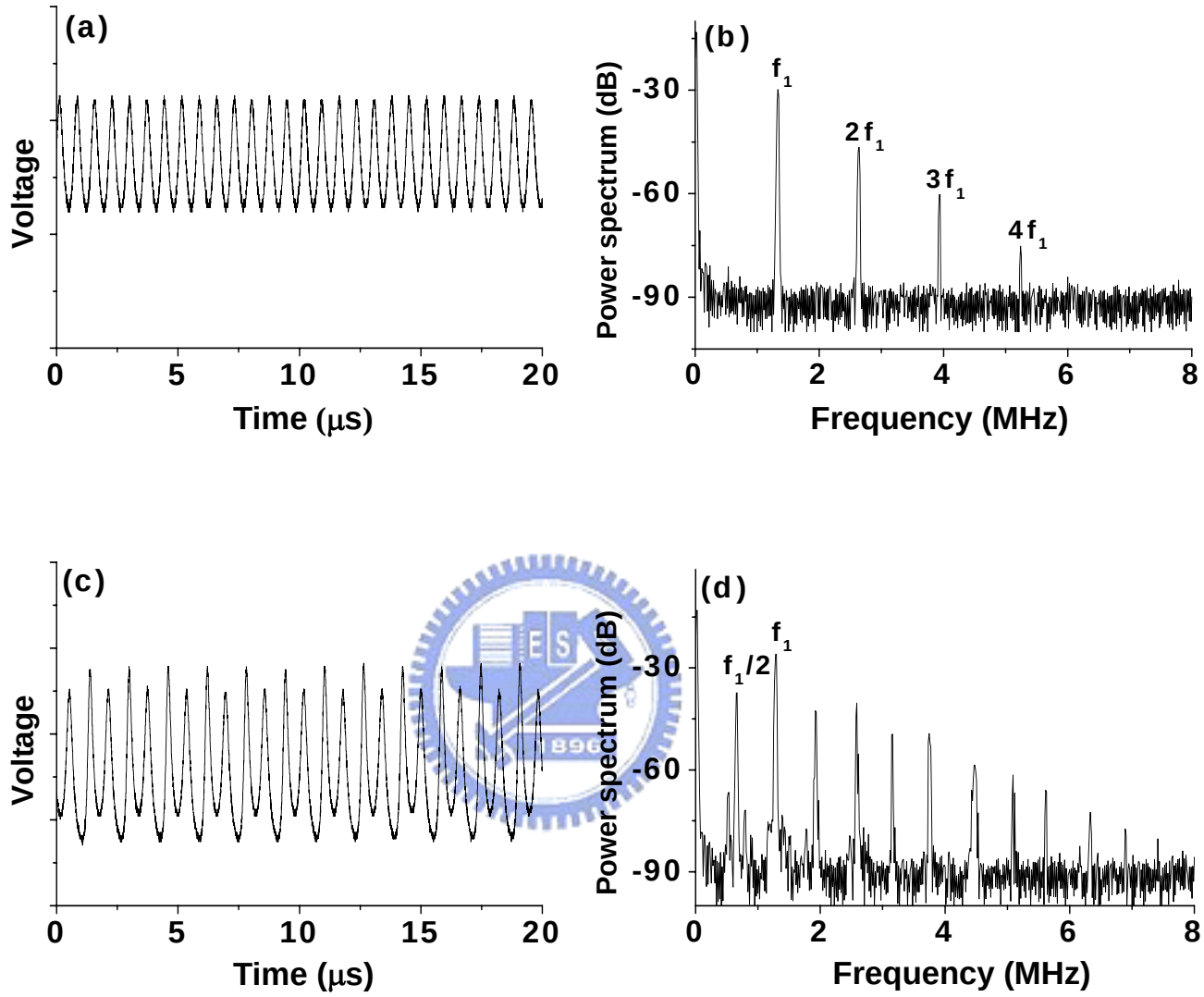


Fig. 4.4. The temporal evolution of laser output. (a) periodic and (c) period-doubled. The RF spectra (b) and (d) correspond to (a) and (c), respectively.

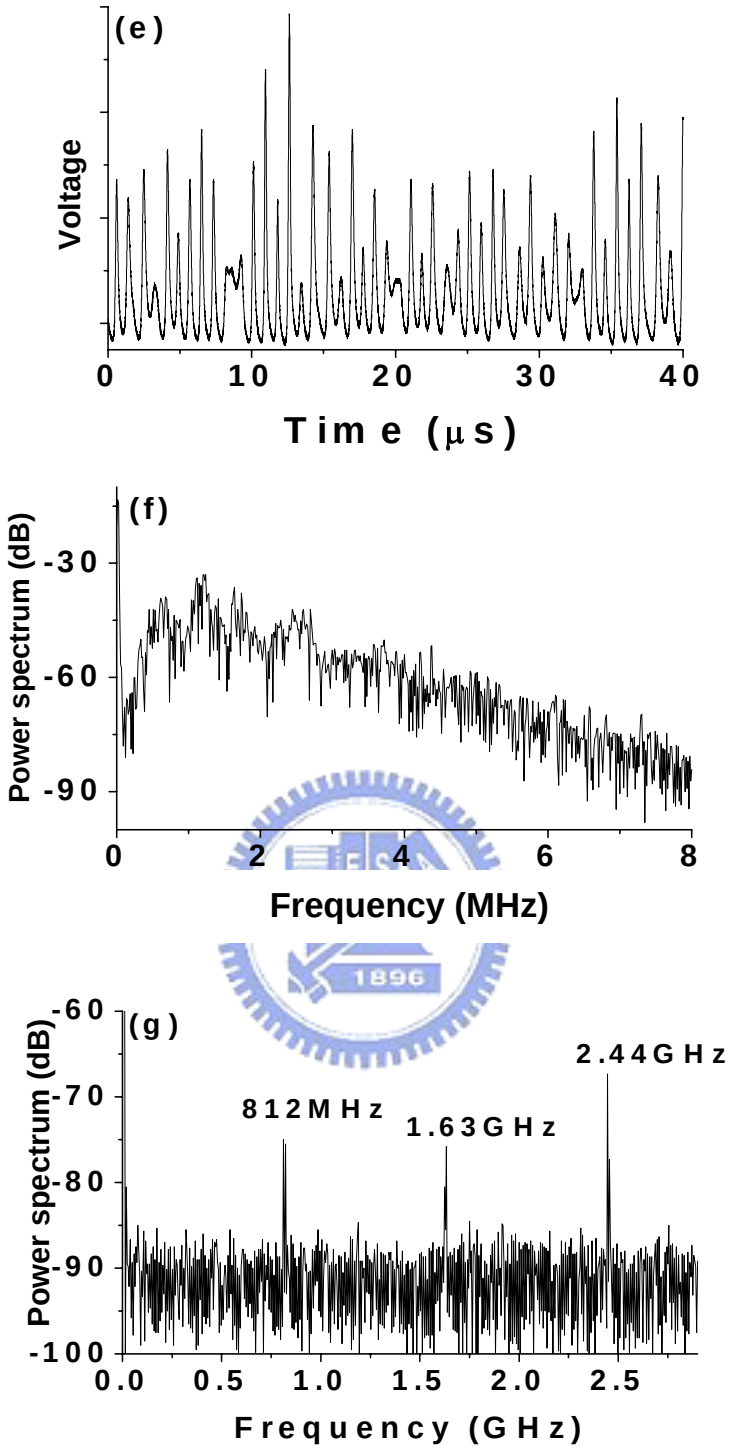


Fig. 4.4 (e) The chaotic temporal evolution of laser output and its RF spectra (f). (g) The high frequency RF spectrum of the spreading mode pattern of Fig. 4.3(a).

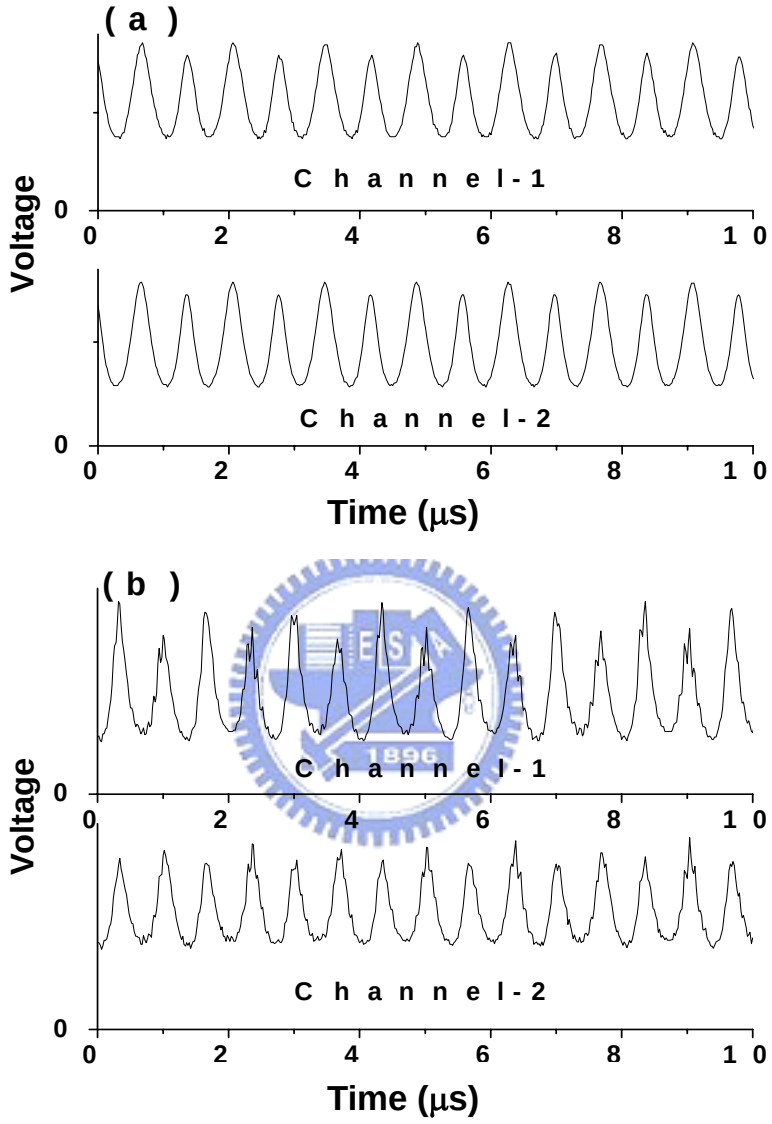


Fig. 4.5. The time traces in oscilloscope when the two PDs are separated close to each other (a) and farther away (b) for the long-cavity instabilities.

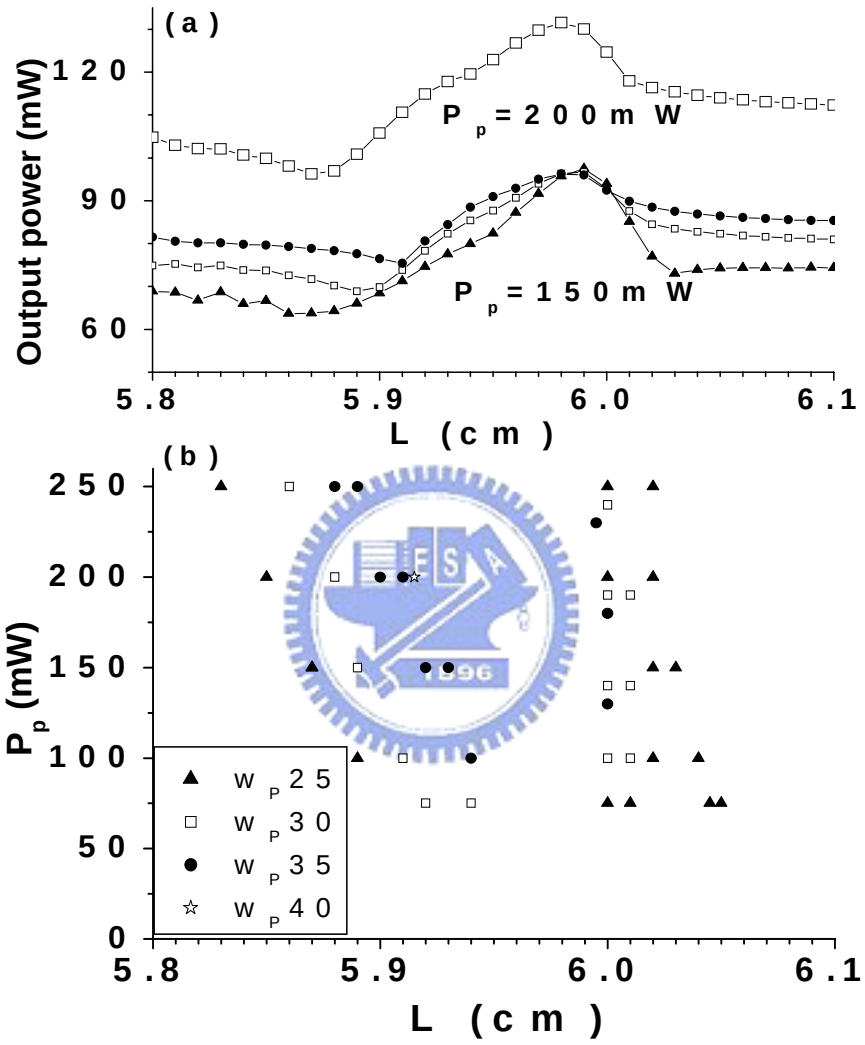


Fig. 4.6. The numerical output power as a function of cavity length with considering the thermal lens effect (a) and the unstable regions (b) for different $w_p$. The symbols for $w_p$ are the same for (a) and (b).

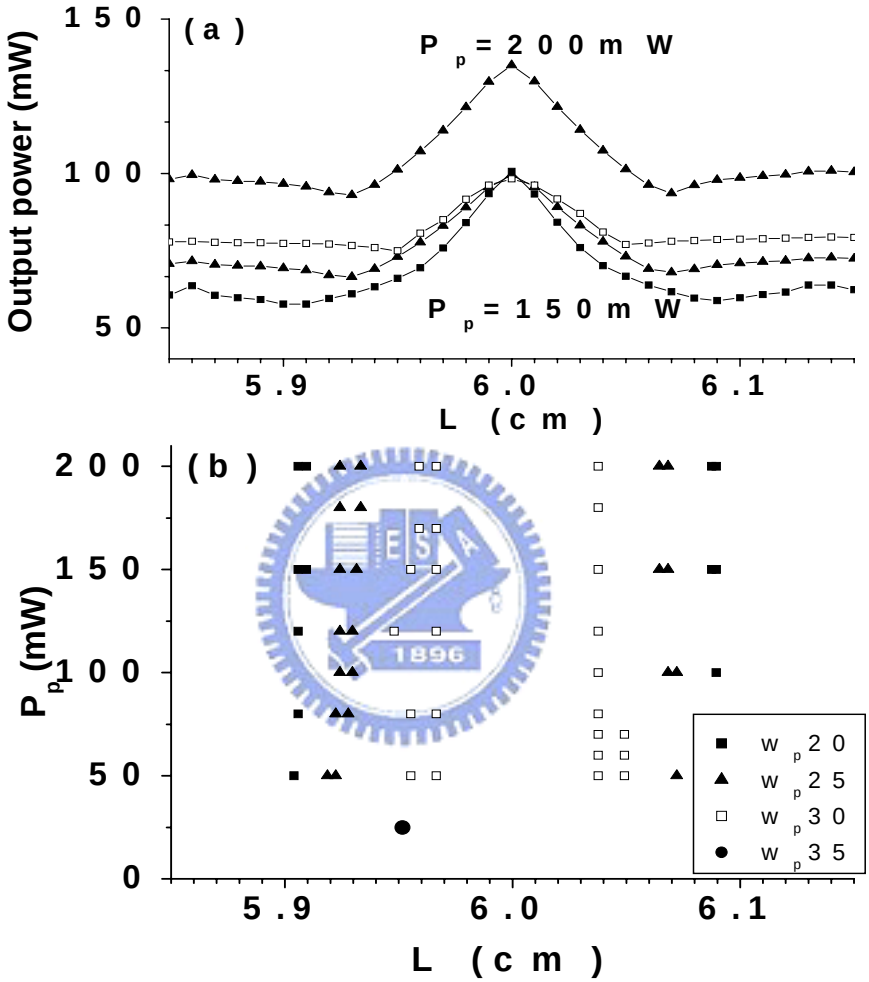


Fig. 4.7. The numerical output power as a function of cavity length (a) and the unstable regions (b) without considering the thermal lens effect. The symbols for $w_p$ are the same for (a) and (b).

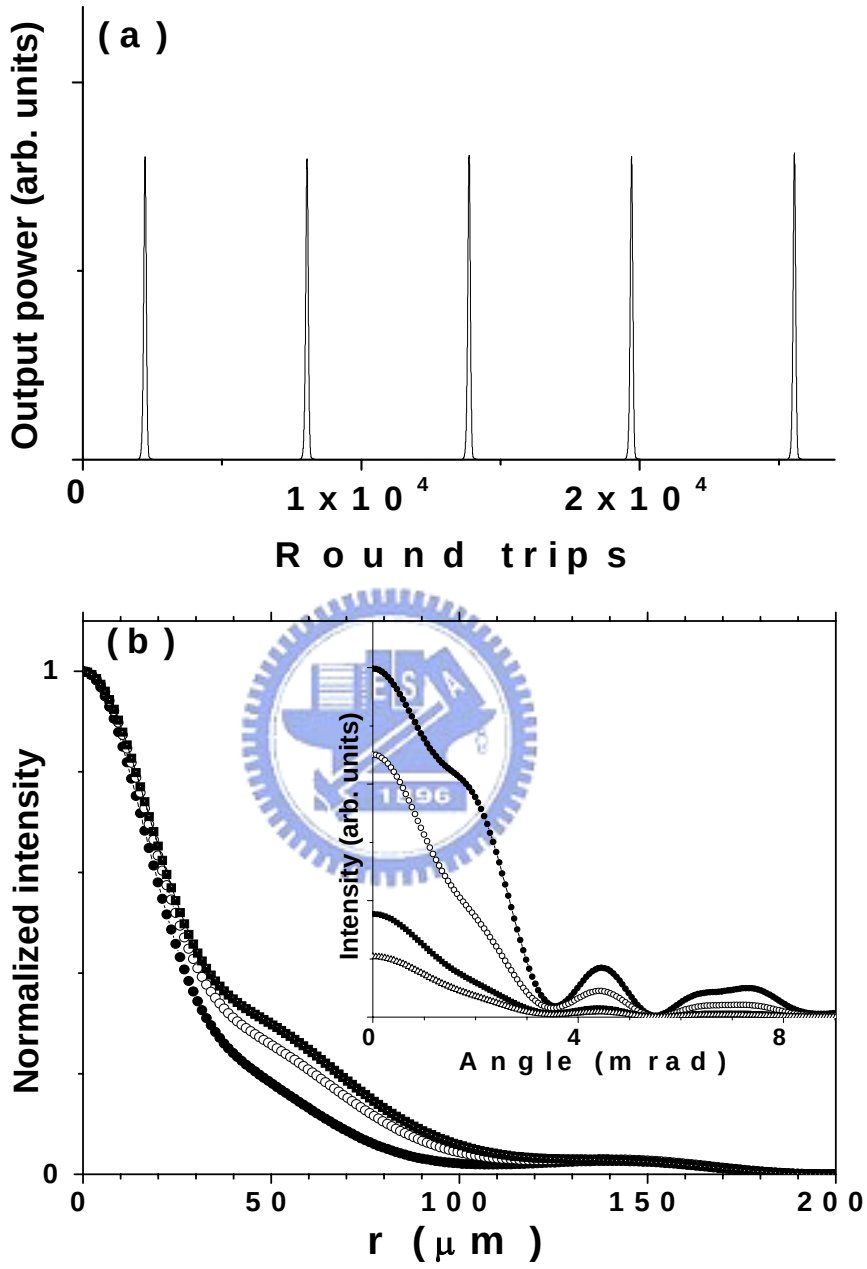


Fig. 4.8. (a) A self-pulsing temporal evolution of the simulated output power without the thermal lens effect. (b) The normalized intensity profiles and their corresponding far-field profiles (inset) from the pulse peak (solid circles) changes to open circles, solid squares and then to the pulse valley (open triangles). The normalized profiles of the open triangles are covered by the solid squares. The modal analysis for the profile of solid squares are $LG_{0,0}$ ($0^o$)+ 0.63 $LG_{3,0}(-75^o)$ + 0.34 $LG_{6,0}(-105^o)$ + 0.16 $LG_{9,0}(-90^o)$ + 0.08 $LG_{12,0}(-83^o)$ + 0.08 $LG_{15,0}(-116^o)$ + 0.07 $LG_{18,0}(-93^o)$.

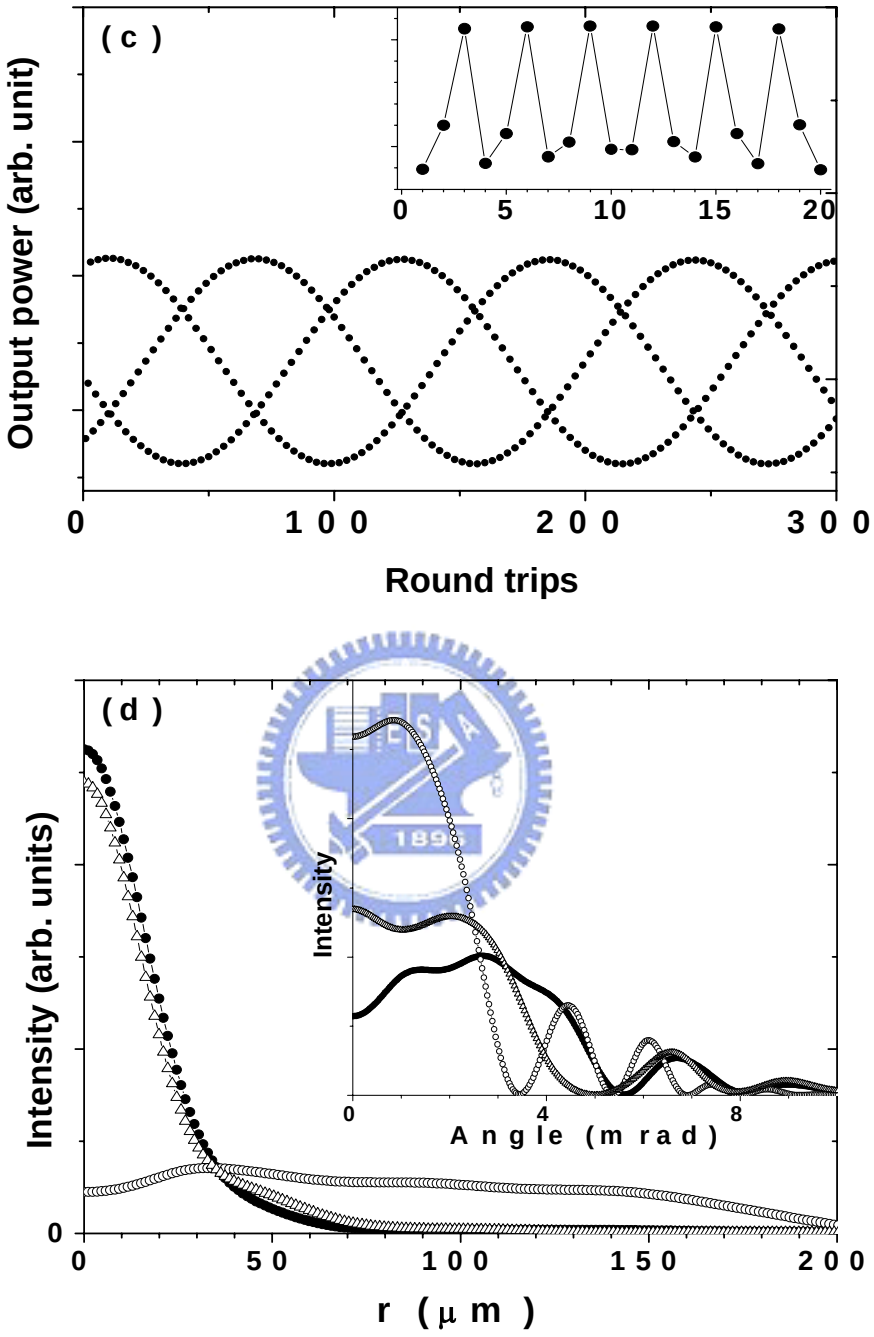


Fig. 4.8 (c) The numerical temporal evolution of the output power in the vicinity of the degeneracy with the thermal lens effect for L = 6.005 cm. Inset is the first 20 iterations. (d) The intensity profiles and their corresponding far-field profiles (inset) of three successive round trips.

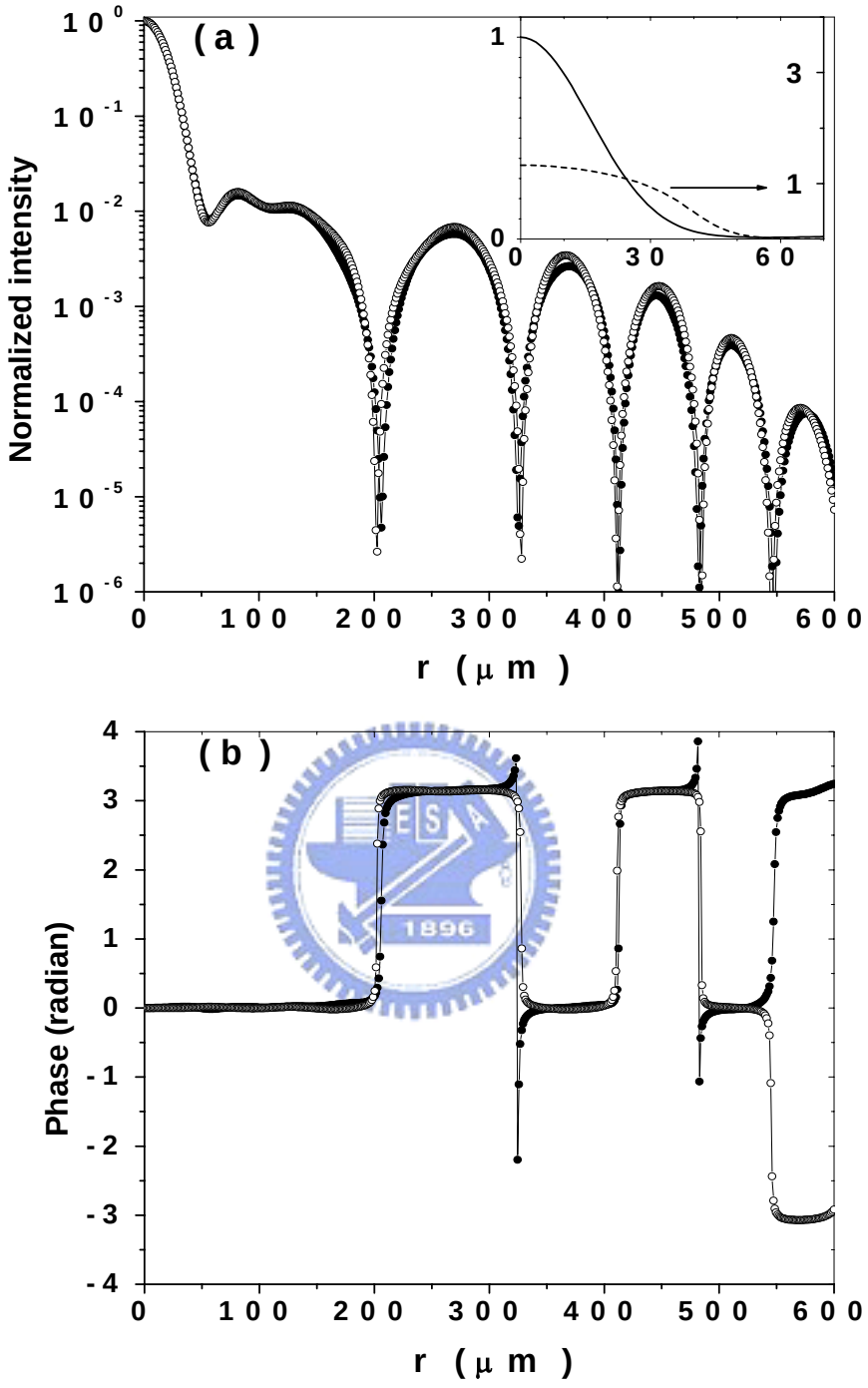


Fig. 4.9. The intensity profile (a) and the phase pattern (b) for the exact degeneracy at L = 6.0 cm for the mode-calculation solution (solid circles) and the fitted mode expansion (empty circles). Inset in (a) are the intensity profile (solid curve) with linear scale and the gain distribution (dashed curve).

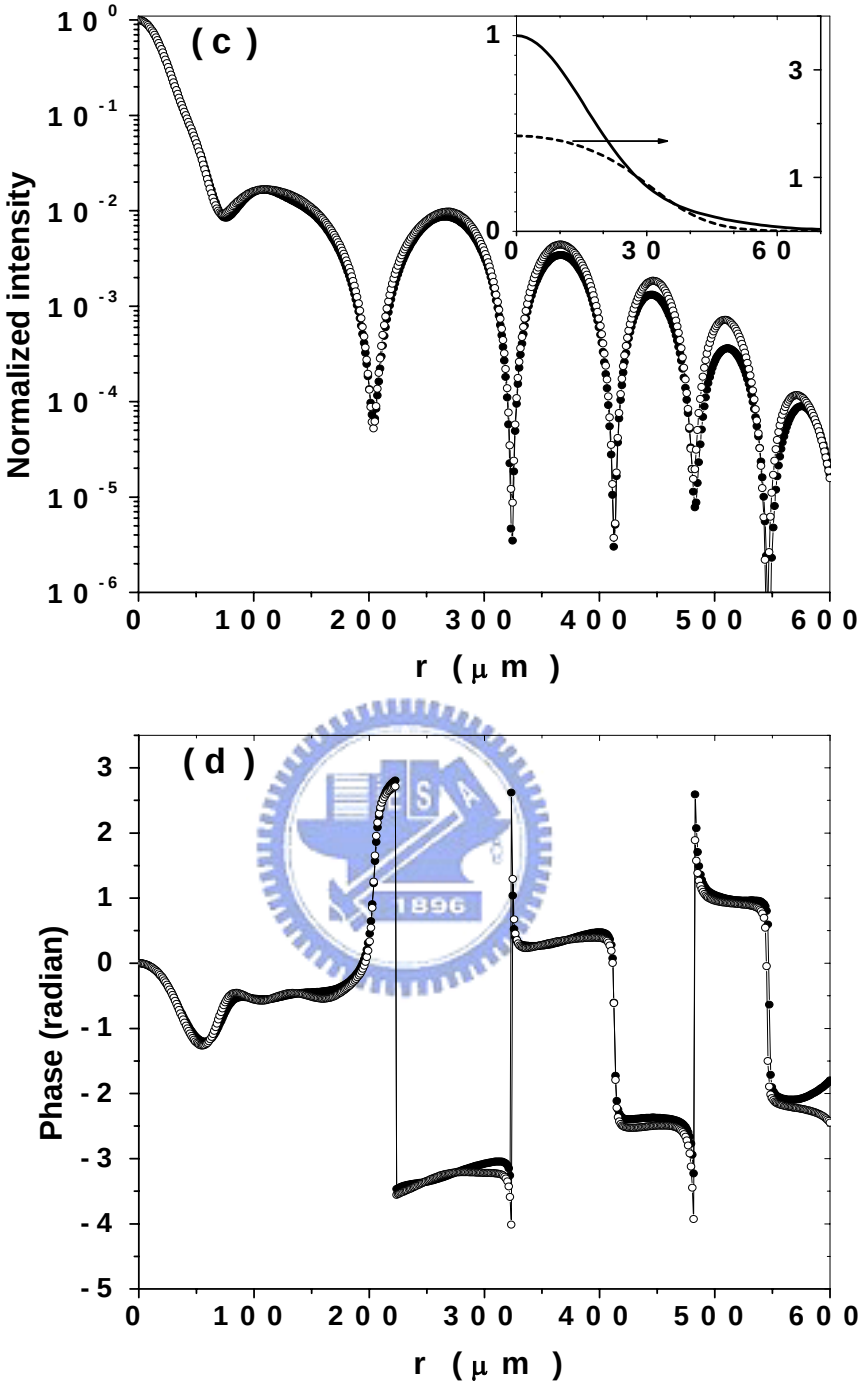


Fig. 4.9 (c) The intensity profile and (d) the phase pattern for L = 6.01 cm. The mode-calculation solution (filled circles) and the fitted mode expansion solution (open circles) match well. Inset of (c) are the intensity profile (solid curve) with linear scale and the gain distribution (dashed curve).

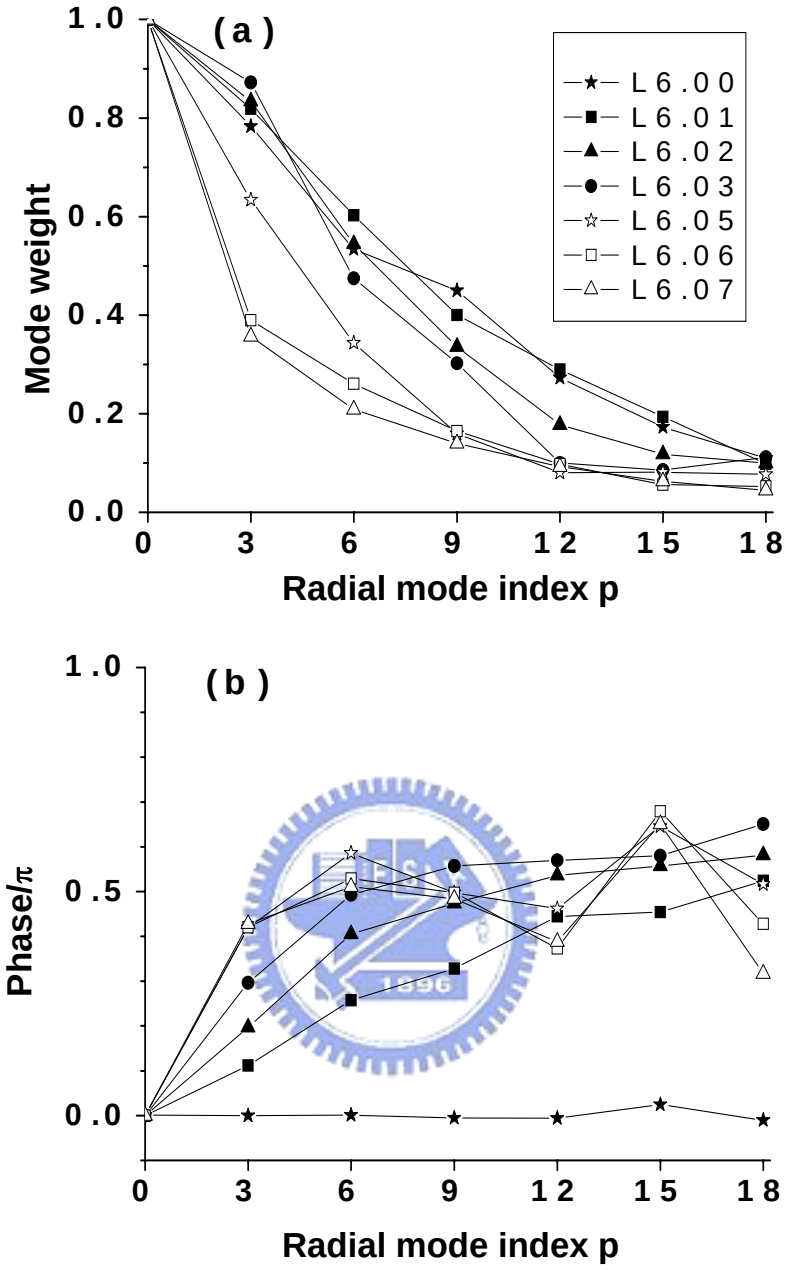


Fig. 4.10. The mode weight ratio (a) and the relative phase shift (b) of the empty-cavity $LG_{p,0}$ modes as L is tuned away from the degeneracy.

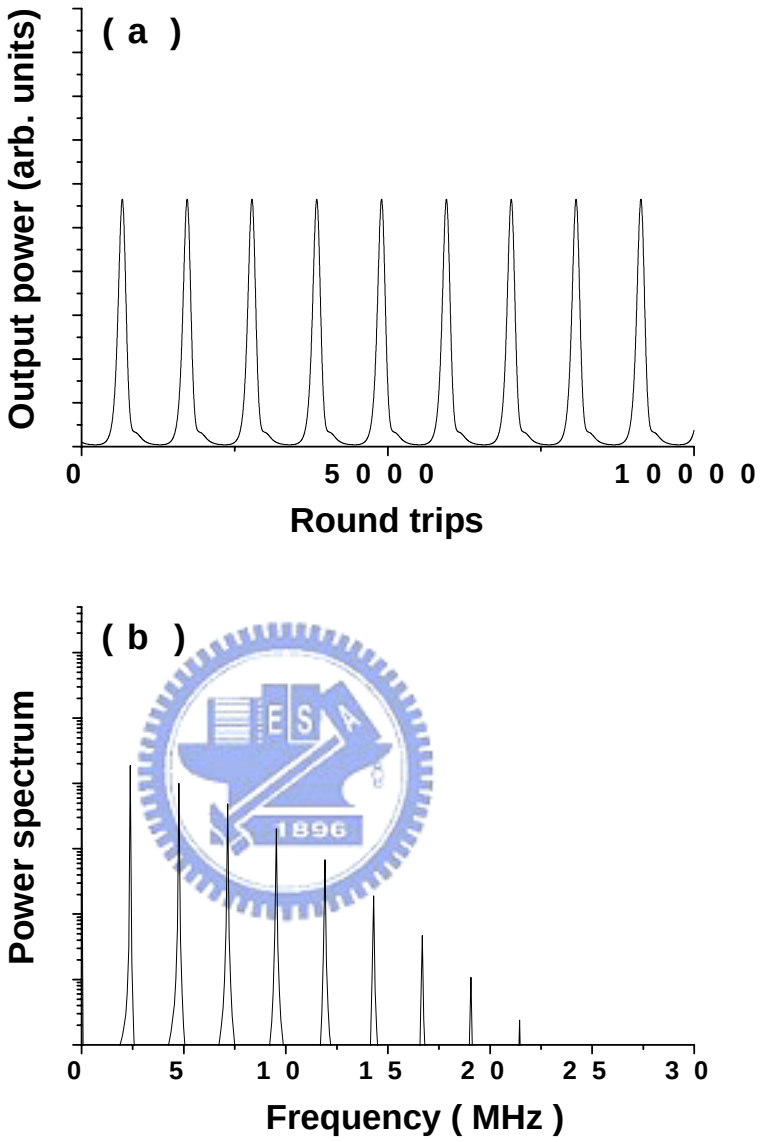


Fig. 4.11. Periodic self-pulsing (a) and its spectrum (b) for L = 5.955 cm.

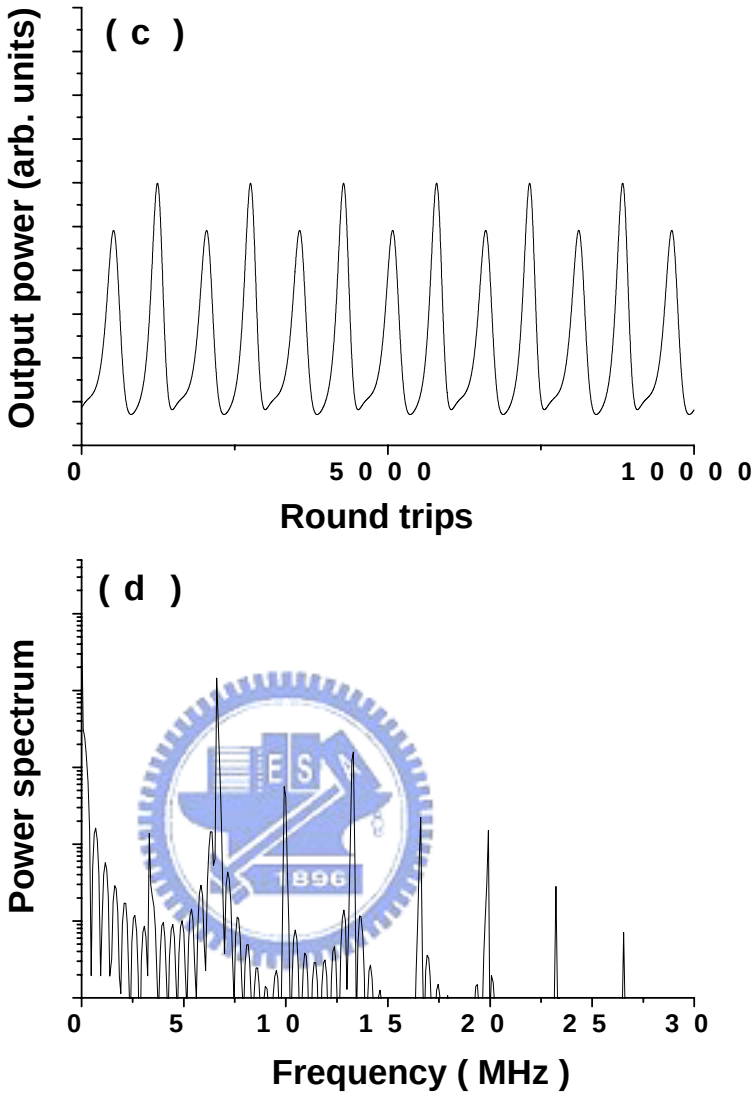


Fig. 4.11 (c) Period-2 self-pulsing and (d) its spectrum for L = 5.9523 cm.

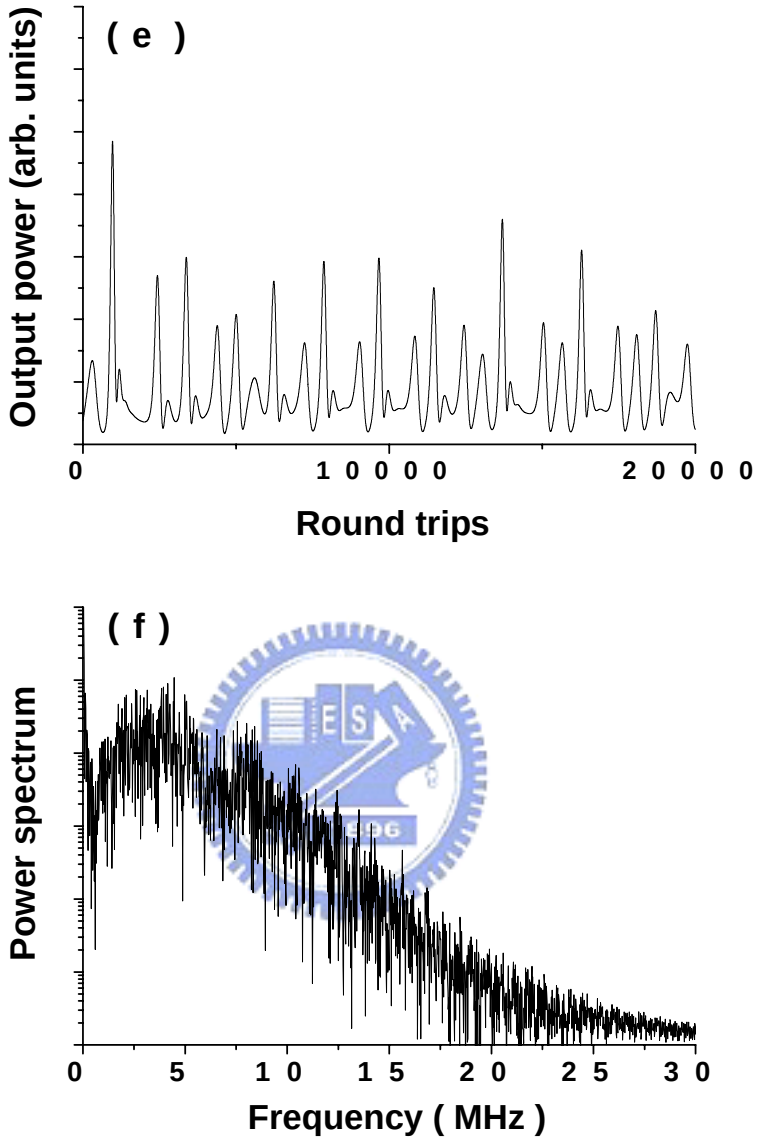


Fig. 4.11 (e) Chaotic output power and (f) its spectrum for L = 5.9505 cm.

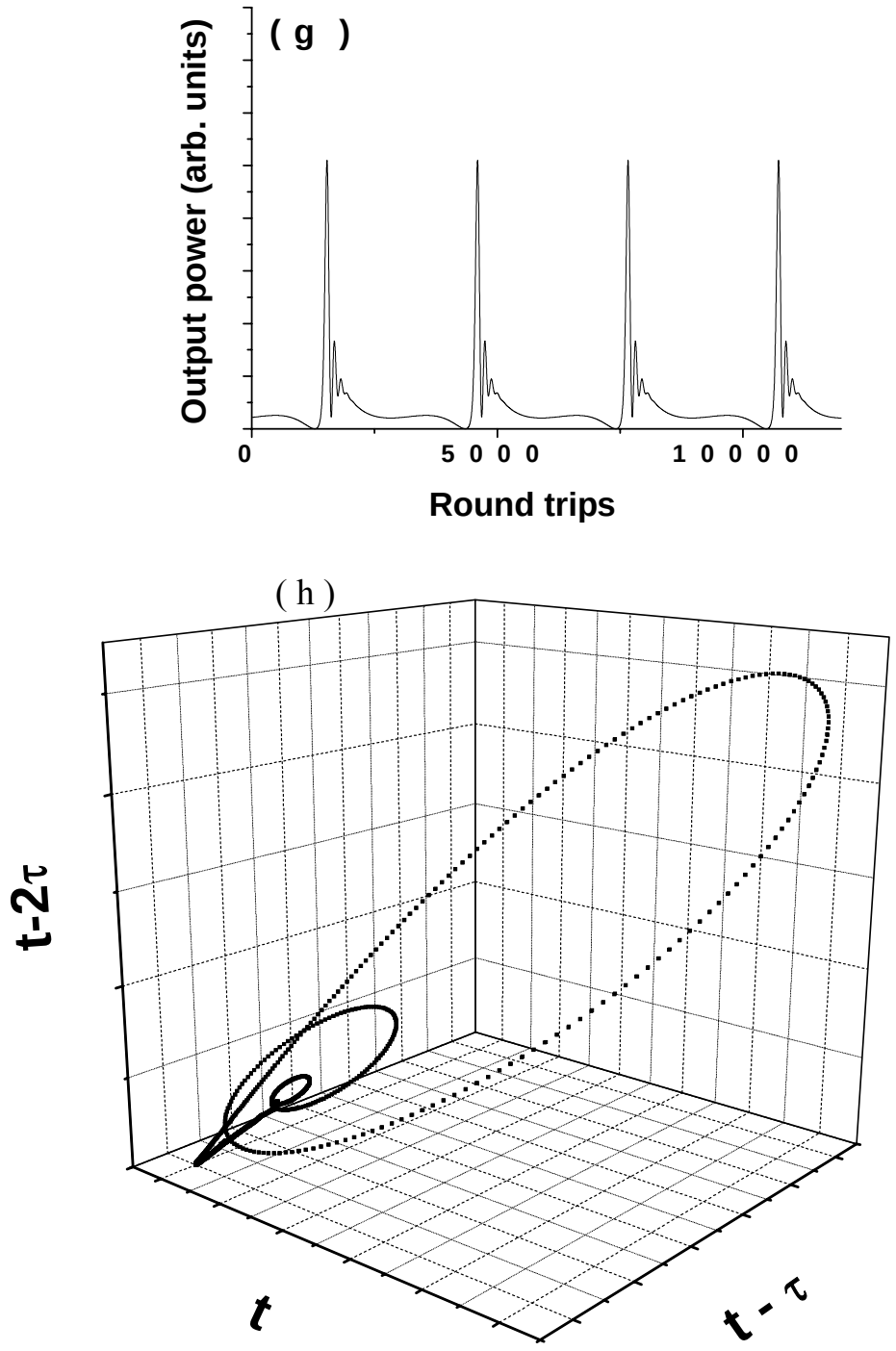


Fig. 4.11 (g) An output power evolution associated with a homoclinic orbit. (h) Phase portrait of a homoclinic orbit. τ is chosen 20 iterations.

## Chapter 5 Conclusions

### 5.1 Summary

Numerically propagating a cavity field through Collin's integral and using the rate equations for a homogeneous broadened gain medium with Gaussian pumping, we obtained propagation-dominant laser instabilities when the pump size is larger than the fundamental Gaussian beam waist size under the high-Q cavity (good cavity) condition. We have investigated in detail on the temporal behaviors of the instabilities near the 1/3-degenerate configuration. We determined the quasi-periodic threshold as the cavity was tuned across the degenerate configuration. A laser with a good cavity including a saturated gain medium shows a V-shaped quasi-periodic threshold; however, a high-loss cavity has not a V-shaped but a smooth monotonic curve. Furthermore, the propagation-dominant V-shaped threshold depends not only on the resonator configuration but also on the pump size. There is a best value $\Psi$ in good cavity to produce the lowest-instability pump power. In addition to a quasi-periodic region, we obtained another region of the propagation-dominant instability outside the chaotic region near the 1/3-degenerate configuration in the good cavity conditions. We ascribed this type of instability to the special dependence of the geometrical configuration.

Furthermore, chaos was found in a good cavity close to the 1/3-degenerate configuration. Although the phase shift between adjacent transverse modes in one round trip is irrational multiples of $\pi$ and lies close to $2\pi/3$, the laser output can become chaotic in a good cavity under Gaussian pumping. This result is different from the results of Hollinger et al. We believe that, as the cavity is tuned toward 1/3-degeneration, the beam-propagation-dominant laser dynamics is transformed into an interplay of beam propagation and gain dynamics. Thus the route to chaos close to the degenerate configuration involves the mixing effect of the quasi-periodic and

period-multiplying bifurcation.

When the pump size is sufficient less than the fundamental Gaussian beam-waist size, we have demonstrated that a laser mode is capable of exhibiting N beam waists when it is propagated through a transform lens, where N = 2 corresponds to $g_1g_2 = 1/2$ and N = 3 to $g_1g_2 = 1/4, 3/4$ with plano-concave cavity. For $g_1g_2 = 1/4$ the multibeam-waist mode has an additional waist close to the curved mirror end; similarly, for $g_1g_2 = 3/4$ one can detect an additional waist outside the cavity without using a transform lens. It is easier to excite the multibeam-waist mode with a smaller pump size because of the stronger gain-guiding effect near specific degenerations within a certain range of cavity tuning. The multibeam-waist mode has a small beam-waist size that is close to the pump size in the near field at the flat mirror end; however, its far-field pattern has a concentric-ring structure. The gain guiding effect dominates the formation of a transverse mode pattern near degeneracy; nevertheless the diffraction effect is more important away from degeneracy.

Moreover, by simultaneously considering the wavelike and the raylike characteristics of the multibeam-waist mode we expand the mode as a superposition of N consecutive electric fields of period-N solution but not for the orthogonal bases. Because these N fields act as independent in-phase sources located in different positions with different waist sizes, the mode can converge to form N beam waists at different positions after the transform lens. The beam profile variation with propagation distance, in particular those profiles with low intensity on the axis, is well simulated. The additional waist in the absence of a transform lens is due to the convergence of the field with negative curvature of the period-N solution. The ring pattern in the far field or in any position is the result of interference of the N consecutive round-trip electric fields. Because the axially pumped solid-state lasers are widely used, the multibeam-waist modes may be important because there are

many degenerate positions within the geometrically stable region.

Also due to small-size pumping, we have found the new transverse instabilities and determined the unstable regions on each side of the degeneracy near $g_1g_2 = 1/4$. We illustrated the temporal behaviors including periodic self-pulsing, period-2 self-pulsing, and chaotic output. Various far-field patterns beside the unstable regions were observed; in particular, an asymmetrical mode pattern was observed in the vicinity of the degeneracy. Our numerical results agree well with the experiments and reveal the influence of the thermal lens effect. As far as we know, this is the first time to discuss the relationship between the instability and the thermal lens effect. In the short-cavity side a supermode that interacts with the inverted population leads to the temporal instabilities. However, the spatiotemporal instability in the long-cavity side arises mainly from the frequency beating between the supermode and the other empty-cavity modes.

## 5.2 Suggestions for future work

Because the laser instabilities induced by the wide pump have been numerically studied, the experimental investigation is the first work we can do. The second is to clear out whether the cavity-configuration-dependent instabilities induced by a small pump size are associated with a homoclinic orbit. Moreover, the transverse mode locking has been obtained from calculations and then we can determine the exact locking range of cavity length detuning by experiments. The transverse mode locking leads to the phase pattern of the transverse modes depending sensitively on the cavity configuration near degeneracies, which in turn results in the Petermann K factor being cavity-configuration-dependent. So we can take into account the thermal lens effect to calculate the Petermann K factor and we can do an experiment to detect the excess noise. Finally, the MBW mode is potential to be used in optical

trapping since there are three waists in the proximity of the beam focus. One may try the single MBW beam to trap high-index particles in multiple axial sites.